Obrabotka metallov (tekhnologiya, oborudovanie, instrumenty) = Metal Working and Material Science. 2026 vol. 28 no. 3 pp. 205–228
ISSN: 1994-6309 (print) / 2541-819X (online)
DOI: 10.17212/1994-6309-2026-28.3-205-228

NSTU NETI

Obrabotka metallov -
Metal Working and Material Science

Journal homepage: http://journals.nstu.ru/obrabotka_metallov

Determination of the relationship among the structure, properties and strain state of the 0.09C-2Mn-Si steel under tension

Yulia Khudorozhkova [1, a, *], *Sergey Burov* [1, b], *Anna Povolotskaya* [1, 2, c], *Dmitry Vichuzhanin* [1, d]

[1] Institute of Engineering Science, Ural Branch of the Russian Academy of Sciences, 34 Komsomolskaya St., Ekaterinburg, 620049, Russian Federation
[2] M.N. Mikheev Institute of Metal Physics of the Ural Branch of the Russian Academy of Sciences, 18 S. Kovalevskoy St., Ekaterinburg, 620108, Russian Federation

[a] https://orcid.org/0000-0003-3832-1419, khjv@mail.ru; [b] https://orcid.org/0000-0002-0413-1054, burchitai@mail.ru;
[c] https://orcid.org/0000-0002-8301-5069, anna.povolotskaya.68@mail.ru; [d] https://orcid.org/0000-0002-6508-6859, mmm@imach.uran.ru

ARTICLE INFO

Article history:
Received: 14 June 2026
Revised: 23 June 2026
Accepted: 11 July 2026
Available online: 15 September 2026

Keywords:
Plastic deformation
Uniaxial tension
Fracture site
Deformation relief
Degree of deformation
Deformation modeling
Surface roughness

Funding
This work was carried out within the framework of state assignments from the Ministry of Science and Higher Education of the Russian Federation to the Institute of Mechanical Engineering, Ural Branch of the Russian Academy of Sciences (topic no. 124020700063-3) and the M.N. Mikheev Institute of Metal Physics of the Ural Branch of the Russian Academy of Sciences (topic "Diagnostics", no. 122021000030-1).

Acknowledgments
This work was carried out using equipment from the "Plastometry" Collective Use Center at the Institute of Mechanical Engineering, Ural Branch of the Russian Academy of Sciences, and the "Structure, Mechanical, and Physical Properties of Materials" Collective Use Center at Novosibirsk State Technical University. To assess the stress–strain state during deformation, a specimen model was constructed in the ANSYS finite element analysis package, and tensile testing was simulated. The calculations were performed on the "Uran" supercomputer at the N.N. Krasovskii Institute of Mathematics and Mechanics of the Ural Branch of the Russian Academy of Sciences.

ABSTRACT

Introduction. Although structural transformations during plastic deformation are well studied, they remain a priority area of scientific research in the field of materials science. Different approaches converge on the fact that metal deformation develops from the microscale to the macroscale level and that the change in stages is an abrupt loss of structural stability, which inevitably ends with localization of shear and failure in the neck. ***The purpose of this study*** was to determine the relation of the plastic deformation stages to the structure, surface topography and micromechanical properties of a common structural material, namely grade *0.09C-2Mn-Si* steel, subjected to uniaxial tension. **Materials and methods.** In this study, dumbbell-shaped flat specimens of *0.09C-2Mn-Si* structural steel were studied before and after uniaxial tension. The tension process was simulated by the finite element method, and the distribution of the stress-strain state parameters was obtained. The structure was studied by optical and scanning electron microscopy. The surface roughness parameters were determined by optical profilometry. Kinetic microindentation was used to determine the micromechanical characteristics. **Results and discussion.** A direct correspondence is established among the roughness parameters, deformation stage, and strain level for the *0.09C–2Mn–Si* steel. It is found that the strain values are the highest near the crack, that the structure contains no pronounced pearlite colonies, and that there are elongated ferrite grains with boundaries sometimes decorated by fragmented cementite plates. Strain-induced discontinuities and elongated pores are clearly visible. The surface relief is caused by the sliding of meso- and macrobands. The relationship between the mechanical properties of the steel and the structures obtained at various stages — from the onset of plastic deformation up to macrocrack formation — is analyzed. It is shown that the combined use of optical profilometry, structural characterization methods, and micromechanical tests during instrumented indentation enables reliable recording of structural changes in various regions of *0.09C–2Mn–Si* steel specimens after static loading.

For citation: Khudorozhkova Yu.V., Burov S.V., Povolotskaya A.M., Vichuzhanin D.I. Determination of the relationship among the structure, properties and strain state of the 0.09C-2Mn-Si steel under tension. *Obrabotka metallov (tekhnologiya, oborudovanie, instrumenty) = Metal Working and Material Science*, 2026, vol. 28, no. 3, pp. 205–228. DOI: 10.17212/1994-6309-2026-28.3-205-228. (In Russian).

*** Corresponding author**
Khudorozhkova Yulia V., Ph.D. (Engineering)
Institute of Engineering Science,
Ural Branch of the Russian Academy of Sciences,
34 Komsomolskaya St.,
620049, Ekaterinburg, Russian Federation
Tel.: +7 904 387-50-59, **e-mail:** khjv@mail.ru

Introduction

The extensive body of research on the strain hardening of metals is confirmed by the abundance of specialized publications, both in Russia and abroad [1–14]. These works analyze in detail the kinetics of the structural evolution accompanying the plastic flow of materials at all its stages. Metallic materials in a single-phase state are often used as model materials, although a number of studies consider the behavior of materials with a heterophase structure during static and fatigue loading [15–20]. The majority of these studies focus on structural changes occurring in metals under static or quasi-static loading at room temperature. Failure under these conditions is predetermined by dislocation slip. It is this mechanism that activates plastic flow and subsequent damage to the structure. In this case, failure is considered as the final stage of plastic flow of the material, caused by the loss of shear stability at the macroscopic level [21–23]. Moreover, at each scale level, plastic flow in the loaded material develops in a localized manner [24, 25]. The initial stage of the process at the microscale is the blocking of deformation defects and the generation of dislocation clusters in slip planes. Further development of deformation leads to its localization at the mesoscale. In [26, 27], the authors associate this stage with the development of shear bands and the formation of non-crystallographic slip zones, which are generated by intergranular stress concentrators. At the same time, study [28] demonstrates the role of double helices of localized plastic flow, characteristic of the deformation of nanostructured surface layers. At the macroscale, macrobands of localized plastic flow are formed. Since the average level of applied loads does not lead to an instantaneous rearrangement of the entire volume of the material, plastic shear occurs as a sum of discrete shifts, taking the form of localized structural transformations. Each spatial scale of deformation localization corresponds to a strictly equivalent class of stress concentrators. The structural transformations themselves are strictly limited by the deformation space: they are clamped either within the microscopic cores of dislocations or within the boundaries of mesoscopic bands of localized flow.

Papers by three groups of authors [1–5, 7–10, 29] contain scaling of the stress–strain curve. The papers by Academician *V.E. Panin* and his co-authors distinguish three stages of deformation caused by three types of shear. The works by *N.A. Koneva* and her co-authors identify five stages of deformation caused by changes in the deformation structure. In the work by *L.B. Zuev* and *Yu.A. Khon*, deformation is divided into four stages, mentioning that it occurs due to localization in individual zones. Although the authors describe the same physical process, they use different physical approaches. Despite calling the stages of deformation differently and paying attention to different structural changes, all authors agree that deformation does not occur at a single level; the process develops from micro- to macroscales. These approaches agree that the structures arising at different stages of deformation obey the laws of scale invariance, and a change of stages on the stress–strain curve is always a moment of restructuring of the localization geometry: a change in the type of dislocation structure, a change in the type of autowave, or a change in the scale level. The transition from one stage of hardening to another on the deformation curve is interpreted by all authors as a loss of stability of the current structure. When a dislocation structure, mesovolume, or autowave exhausts its ability to accumulate energy without changing its shape, the system jumps to a new energy and scale level, which is reflected in a change in the slope of the deformation curve. All three models interpret the macrofracture of a sample in the same way: as a global, critical localization of shear in one fixed zone (neck). Fracture is interpreted as the inevitable finale of the evolution of the structure, when plastic flow loses its ability to be distributed throughout the volume of the material.

According to the authors of [29], a shortcoming of most existing studies is the insufficient focus on the macroscale effects of plastic flow arising from the non-equilibrium and nonlinearity of the deformed medium. Instead, research mainly focuses on the evolution of the material structure at the mesoscale during deformation [30–34].

Thus, when diagnosing the deformation history of a real material based on mechanical, micromechanical, and structural studies, researchers need to clearly correlate the deformation stages with the structural, topographic, and strength properties of the material. In this regard, investigating the macroscopic effects of deformation at different stages of plastic flow in *0.09C-2Mn-Si* steel and their relationship to structural characteristics remains highly relevant. The authors of this study sought to link the deformation stages to the structure, surface topography, and micromechanical properties of this common structural material subjected to uniaxial tension. As a classic low-alloy steel with a pronounced ferritic-pearlite structure, *0.09C-2Mn-Si* steel is the most widely used material in Russia for critical welded structures. While deformation localization processes at the meso- and macro-levels are most pronounced in this material, their stage-by-stage nature within the three considered concepts has not yet been systematically studied.

To study the structure and micromechanical properties, a combination of methods was used, including optical and scanning electron microscopy, electron backscatter diffraction (*EBSD*), profilometry, and instrumental microindentation. These techniques were chosen to complement each other in capturing the stages of deformation localization: profilometry evaluates the macro- and mesorelief, instrumental microindentation records the evolution of microhardness and mechanical property degradation, while *EBSD* analysis reveals substructural changes and misorientations.

The purpose of this study is to determine the relationship between plastic deformation stages and the microstructure, surface topography, and micromechanical properties of a widely used structural material – *0.09C-2Mn-Si* steel – subjected to uniaxial tension. To achieve this, ***the following objectives*** were formulated:

– to determine equivalent stress and strain distributions in deformed specimens using finite element analysis;

– to characterize the microstructure via optical microscopy, scanning electron microscopy, and electron backscatter diffraction at various strain levels;

– to evaluate micromechanical properties in specimens at various strain levels;

– to investigate deformation-induced surface microrelief evolution using optical profilometry at various strain levels.

Methods

The studies were carried out on flat specimens with a cross-section of 20×4 mm and a gauge length of 100 mm, cut from a sheet of *0.09C-2Mn-Si* low-carbon structural steel (chemical composition in wt.%: 0.073 *C*, 0.680 *Si*, 1.11 *Mn*, 0.066 *Cr*, 0.061 *Ni*, 0.125 *Cu*, 0.039 *Al*, and balance *Fe*). The elemental composition of the specimens was studied by optical emission spectrometry using the *SPECTROMAXx* analytical complex. After cutting and grinding, the specimens were subjected to subcritical vacuum annealing to relieve residual macro- and micro-stresses. This annealing was necessary because *EBSD* analysis, which is sensitive to residual stresses, was carried out before deformation. Annealing was performed in a vacuum furnace at a holding temperature of 580 °C. The holding time was 40 minutes after the furnace reached its operating temperature, which was sufficient to complete the stress relaxation processes without initiating collective recrystallization and ferrite grain growth, which would distort the subsequent *EBSD* analysis results. The residual pressure in the furnace was 10^{-5} mm Hg to prevent oxidation and decarburization of the specimens. The specimens were furnace-cooled. Fig. 1 shows a schematic representation of the specimens before and after tensile testing on an *INSTRON 8801* machine. The crosshead speed was 1 mm/min. Two specimens (1 and 3) were stretched until fracture, and one was stretched until deformation localized into a neck.

For specimens 1 and 3, the maximum opening of a crack approximately 10 mm long was about 0.5 mm.

The tests yielded the following mechanical properties of the steel: physical yield strength R_eL = 350 MPa and ultimate tensile strength R_m = 500 MPa. The resulting engineering stress–strain diagram is shown in Fig. 2. The engineering stress and strain were calculated using formulas (1) and (2): where P is the applied tensile load; F_0 is the initial cross-sectional area; l_0 and l are the initial and current gauge lengths, respectively.

The mechanical properties of the investigated steel, such as the physical yield point R_eL = 350 MPa and the ultimate tensile strength R_m = 500 MPa, were determined from the results of the tests. The engineering stress–strain diagram was also obtained (Fig. 2). Engineering stresses and strains were calculated using the formulas:

$$\sigma = \frac{P}{F_0}, \tag{1}$$

$$\varepsilon = \frac{l - l_0}{l_0} \cdot 100\%, \tag{2}$$

where $\boldsymbol{P}$ is the applied tensile load; $\boldsymbol{F_0}$ is the initial cross-sectional area; $\boldsymbol{l_0}$ and $\boldsymbol{l}$ are the initial and current gauge lengths, respectively.

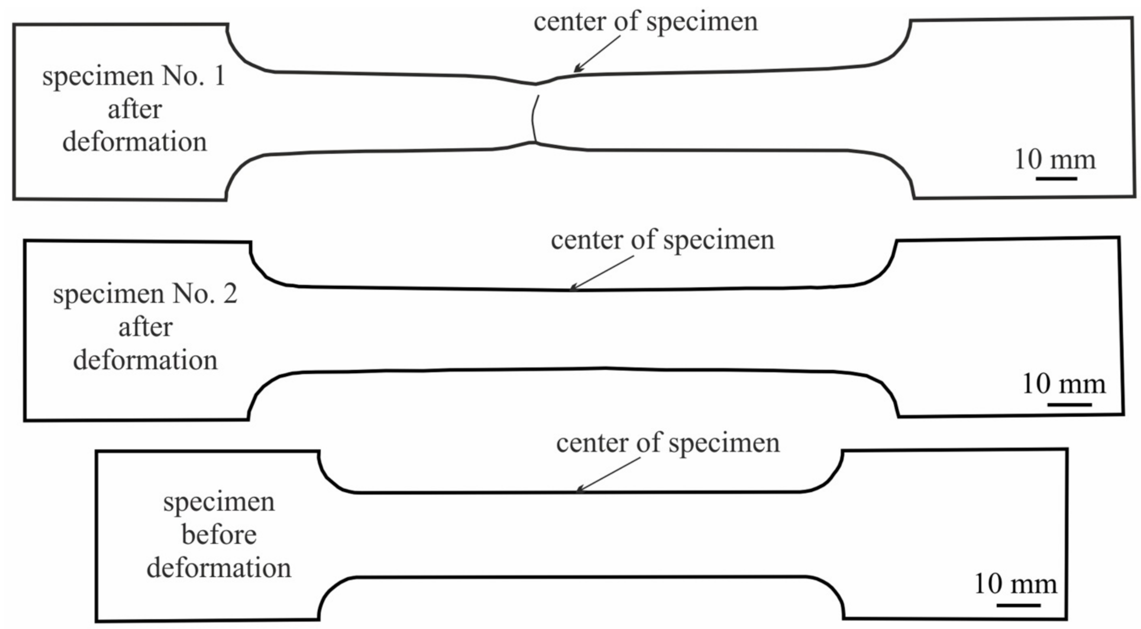

Fig. 1. Schematic of specimens before and after deformation

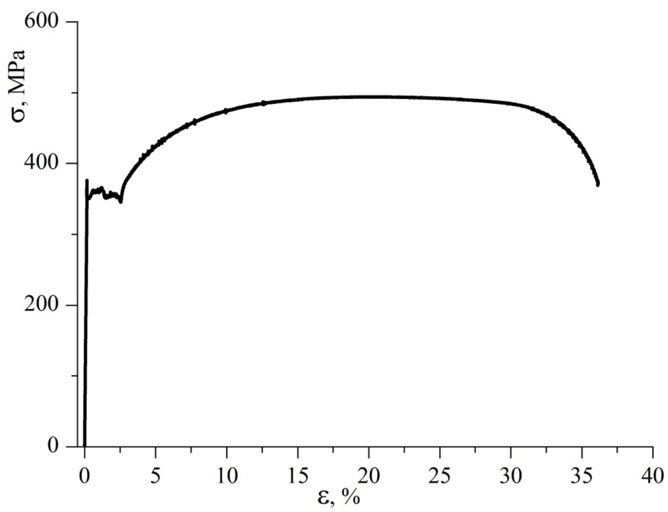

Fig. 2. Stress–strain diagram

The true stresses and strains up to the onset of necking were calculated from engineering stress–strain diagram using the formulas:

$$\sigma_S = \sigma \cdot \left(1 + \frac{\varepsilon}{100}\right); \qquad \varepsilon_{eq} = \frac{2}{\sqrt{3}} \cdot \ln\left(1 + \frac{\varepsilon}{100}\right). \tag{3}$$

To determine the true stress and true strain at fracture, the following formulas were applied:

$$\sigma_S = \frac{P_p}{F_p}; \qquad \varepsilon_{eq} = \frac{2}{\sqrt{3}}\sqrt{\left(\ln\frac{t_0}{t_p}\right)^2 + \ln\frac{t_0}{t_p}\cdot\ln\frac{a_0}{a_p} + \left(\ln\frac{a_0}{a_p}\right)^2}, \tag{4}$$

where t_0 is the initial thickness of the gauge section; t_p is the thickness at the neck at the moment of rupture; a_0 is the original width of the gauge section; a_p is the width at the neck at fracture; P_p is the tensile force recorded at fracture; F_p is the cross-sectional area of the neck determined after the test.

The initial portion of the true stress–strain curve (up to the onset of necking) can then be joined to the point at fracture.

The simulations were performed using the finite element software *ANSYS*. An isotropic elastoplastic model with strain hardening was adopted for the material of the deformed specimen. The finite element mesh consisted of *SOLID185* elements. A mesh convergence study was performed to eliminate the effect of finite element mesh size on the results. The mesh size was varied from 1.8 mm to 0.8 mm, and the corresponding maximum equivalent strain values in the necking region were compared. It was found (Fig. 3) that the difference between the values obtained with the 0.8 mm and 1.0 mm mesh sizes did not exceed 2%. Therefore, an element size of 0.8 mm was adopted for the subsequent calculations. The finite element model consists of 46,598 elements. The true stress–strain curve used in the simulations was determined earlier [35] by converting the engineering stress–strain diagram using Eqs. (3) and (4). An associated flow rule and the *von Mises* yield criterion were used. Boundary conditions were defined in terms of displacements. Since the specimen has a plane of symmetry, only one quarter of the specimen was modeled (Fig. 4,*a*). The strain distribution along the specimen length was determined from the simulation results (Fig. 4,*b* and Fig. 4,*c*).

To verify the validity of the model, the deformation force obtained from the experiment was compared with that calculated in the simulation. The difference between the numerical and experimental results does not exceed 7.2%.

Based on the simulation results (Fig. 4,*b*), strain localization in the specimen occurs at a distance of 20 mm from the minimum cross-section of the neck. Over the rest of the gauge length, the strain is uniformly distributed at approximately 0.2. Furthermore, at a distance of 60 mm from the neck center, the strain begins to decrease, eventually dropping to zero at the distance corresponding to the gripped section, which does not deform during testing. Utilizing the equivalent strain allows for determining the strain state in various sections of the investigated specimens, including the neck zone, and facilitates transitioning from spatial coordinates to the physical stages of plastic flow.

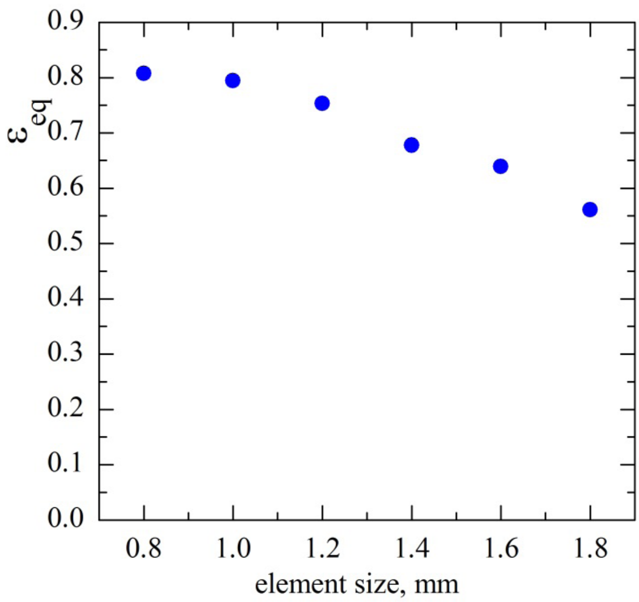

Fig. 3. Results of the mesh convergence study

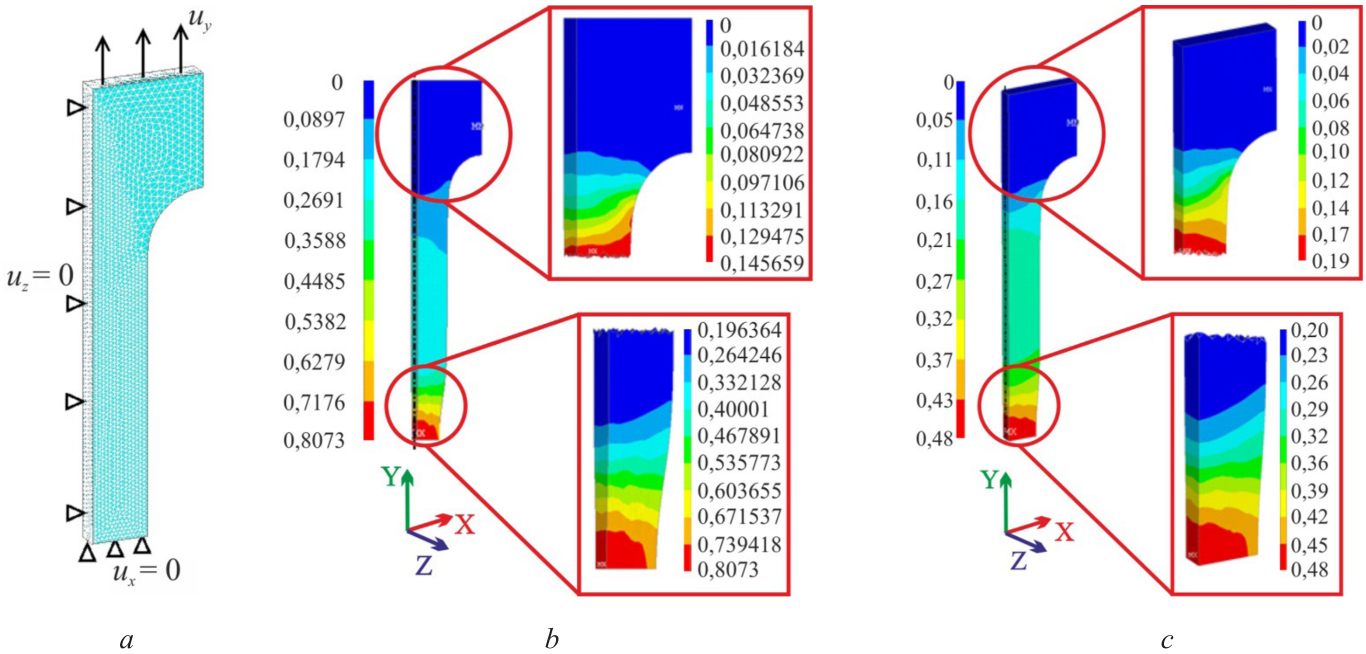

Fig. 4. Finite-element model of the test process (*a*) and strain distribution along the specimen length for specimen 1 (*b*) and specimen 2 (*c*)

Specimen deformation was accompanied by changes in the surface relief. Consequently, roughness evolution was studied within a 1.2 × 0.88 mm field of view using a *Veeco WYKO NT1100* optical profiler. The root-mean-square roughness ***Rq*** and average roughness ***Ra*** were determined, with both parameters calculated over the entire measurement area.

The microstructure was examined using a *Tescan VEGA II XMU* and a *Carl Zeiss EVO 50* scanning electron microscope, as well as an *AmScope* trinocular inverted metallographic microscope.

To investigate the microstructure, micromechanical properties, and crystallographic texture via electron backscatter diffraction (*EBSD*), specimen 1 was sectioned by electrical discharge machining, as shown in Fig. 5,*a*. Microstructural and micromechanical analyses were performed on longitudinal cross-sections at the locations indicated in Fig. 5,*b*. Specimens 2 and 3 were left intact.

Metallographic specimen preparation was performed using standard techniques. The procedure involved sequential wet grinding on silicon carbide (*SiC*) abrasive papers with *FEPA* grit sizes ranging from *P180* to *P2500*, followed by rough polishing using 6 μm and 3 μm diamond suspensions. One surface of specimen

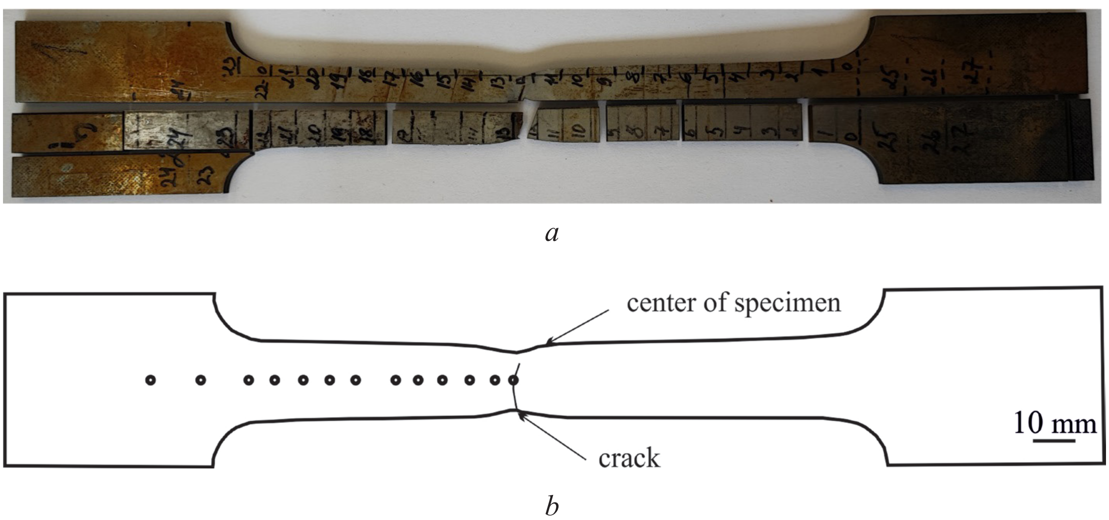

Fig. 5. Cutting scheme (*a*) and locations for metallographic and micromechanical studies (*b*)

3 was then mirror-polished with a colloidal silica suspension (0.05 μm) to achieve a deformation-free state required for electron backscatter diffraction (*EBSD*) analysis. A separate area of the specimen was etched in a 4% Nital solution (nitric acid in ethanol) to reveal the microstructure for optical examination.

Instrumented microindentation with load-displacement curve recording was performed using a *Fischerscope HM2000 XYm* measuring system equipped with a *Vickers* indenter and *WIN-HCU* software. Testing was conducted at a maximum load of 0.98 N, with a loading time of 20 s, a holding time under peak load of 15 s, and an unloading time of 20 s. According to the *ISO 14577* standard, the following parameters were determined: maximum indentation depth h_{max}, residual indentation depth after unloading h_p, contact elastic modulus $E^* = E/(1–\nu^2)^*$ (where E is *Young's* modulus and ν is *Poisson's* ratio), indentation hardness at maximum load H_{IT}, *Martens* hardness HM, elastic indentation work W_e, and total mechanical work of indentation W_t. The uncertainty of the microindentation characteristics was evaluated based on 10–12 measurements per point with a 95% confidence level. The deformation response of the microstructural elements was assessed using the methodology described in [36], which is based on stress–strain curve reconstruction via numerical analysis of the test data and solving the inverse problem.

Results and discussion

The microstructure of the steel studied in its initial state consists of ferrite grains and predominantly lamellar pearlite (Fig. 6). The microstructure also contains tertiary cementite in the form of globules decorating the grain boundaries. The ferrite grain size varies from 5 to 25 μm.

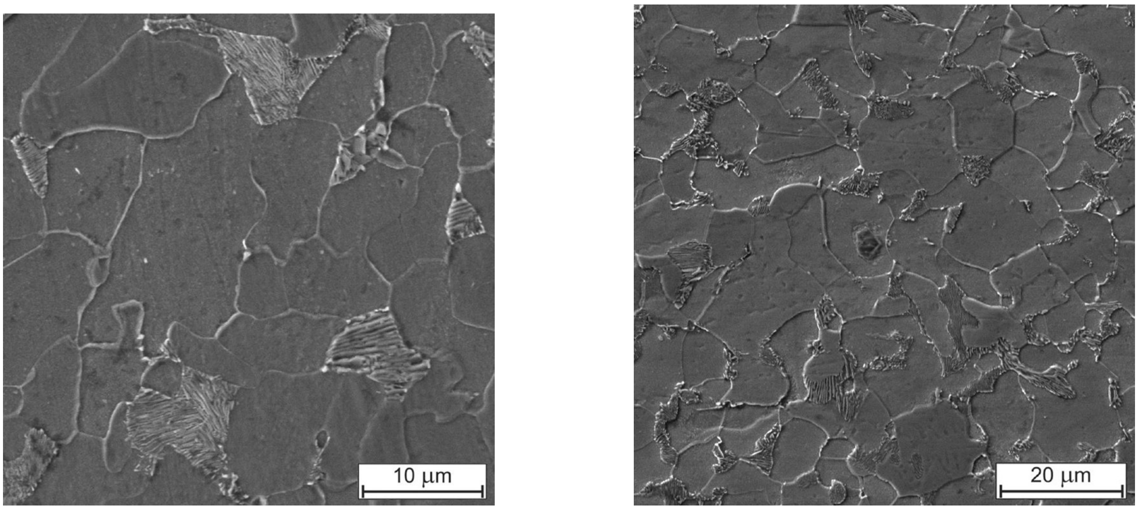

a *b*

Fig. 6. Surface microstructure of specimen 1 (*a*) and specimen 3 (*b*) before deformation

After uniaxial tension, the surface microstructure of specimen 1 near the crack is shown in Fig. 7. Figs. 7,*a* and 7,*b* present the microstructure obtained from a cross-section normal to the surface and oriented along the tensile axis. Near the crack, where the highest strain levels occur, the microstructure lacks distinct pearlite colonies and features elongated ferrite grains, the boundaries of which are occasionally decorated with fragmented cementite platelets. Discontinuities and elongated deformation-induced pores are clearly visible. Fig. 7,*c* illustrates a deformation relief representing the emergence of slip bands at different scale levels, resulting from both the slip of *Lüders–Chernov* macrobands and mesobands within the ferrite grain boundaries. The crack tip and grain elongation are also clearly observable.

The surface microstructures of specimens 2 and 3, subjected to different deformation stages, are presented in Fig. 8. Specimen 2 was loaded up to the initiation of localized deformation, i.e., before the development of a visible neck, while specimen 3 was deformed up to the formation of a macroscopic crack.

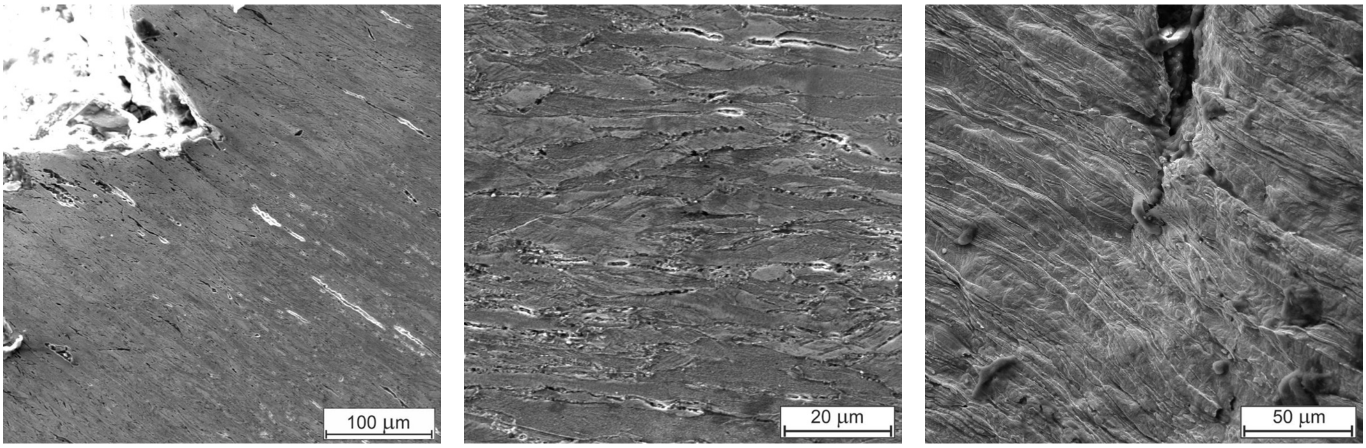

a *b* *c*

Fig. 7. Microstructure of specimen 1 near the fracture site: longitudinal section (*a*, *b*), surface (*c*)

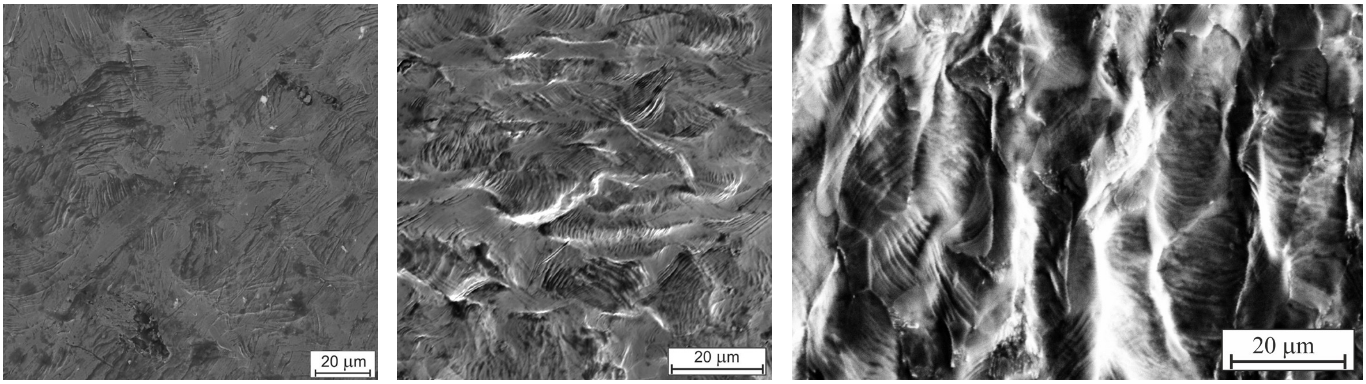

a *b* *c*

Fig. 8. Surface microstructure after deformation: in the center of specimen 2 (*a*), near the fracture site of specimen 3 (*b*, *c*)

Since specimen 2 (Fig. 8, *a*) was subjected to a substantially lower strain level than specimen 3 (Figs. 8, *b* and 8, *c*), its surface relief is less pronounced. Nevertheless, the deformation relief – resulting from dislocation glide in grains favorably oriented with respect to the tensile axis – is clearly discernible. The relief formed by meso-slip bands varies from grain to grain, reflecting the orientation-dependent nature of slip activity.

Upon reaching certain stress levels, the crystal lattice of a given grain begins to rotate about the tensile axis. At moderate and high strain levels, this rotation proceeds non-uniformly within the grain itself. Rotational defects, specifically disclinations, accumulate at grain boundaries and triple junctions, leading to localized rotation of individual crystal volumes within the same grain relative to one another by angles of up to several tens of degrees. As a consequence, large grains become fragmented into misoriented subgrains.

Optical profilometry of the specimen surface along the tensile axis revealed the formation of a deformation-induced macrorelief at a distance of 63 mm from the crack, which became increasingly pronounced with decreasing distance to the crack. Figs. 9 and 10 present the microstructure and corresponding surface topography of the examined areas. These topographic data confirm the non-uniform relief among individual ferrite grains. The microstructures shown in Figs. 9 and 10 indicate that the ferrite grain aspect ratio varies from approximately 1:1 in area 23 to an elongated 6:1 in area 12.

The emergence of defects at the specimen surface, together with the activation of rotational plasticity modes, gives rise to a deformation-induced relief that is inherently associated with changes in surface roughness. Prior to deformation, the roughness values were uniform along the entire specimen length, averaging ***Ra*** = 180 nm and ***Rq*** = 270 nm for specimen 1, ***Ra*** = 180 nm and ***Rq*** = 250 nm for specimen 2, and ***Ra*** = 150 nm and ***Rq*** = 200 nm for specimen 3. The somewhat lower roughness parameters for specimen 3

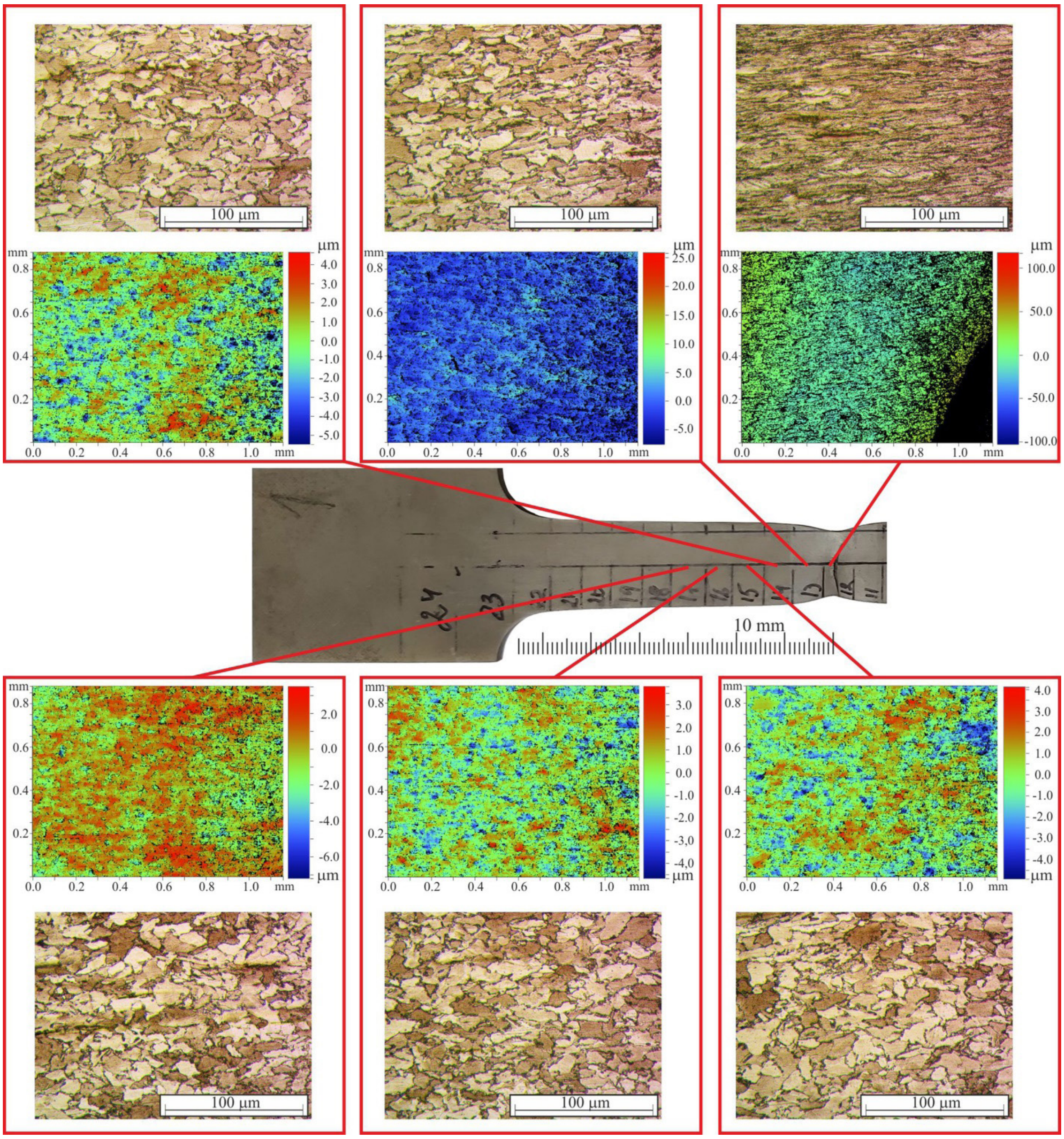

Fig. 9. Microstructure and topographic image of the specimen surface after uniaxial tension at points 2–17

are attributed to the fact that its surface was polished prior to testing using a colloidal silica suspension in preparation for electron backscatter diffraction (*EBSD*) analysis.

The surface topography of specimen 2 before and after tensile deformation is shown in Fig. 11. When compared with the topographies presented in Figs. 9 and 10, the surface relief of specimen 2 (Fig. 11,*b*) exhibits a close resemblance to that of specimen 1 in area 14 (Fig. 9). This finding correlates well with the strain distribution along the specimen length obtained from the modeling results (Fig. 4).

The distribution of equivalent plastic strain, $\boldsymbol{\varepsilon}_{\mathbf{eq}}$, obtained from the numerical simulation along the tensile axis of the specimens, was compared with the surface roughness parameters ***Ra*** and ***Rq***. Fig. 12 presents the evolution of ***Ra*** and ***Rq*** as a function of the distance from the fracture surface for specimens 1 and 3, and from the center for specimen 2. The use of a uniform coordinate step in the plot allowed continuous monitoring of the topographic-deformation response of the material under a spatial stress gradient, ranging from the localized fracture zone to the undeformed region.

In accordance with the theoretical concepts of *L.B. Zuev* and *Yu.A. Khon* [29] (autowave model) and *V.E. Panin* [32] (physical mesomechanics), plastic flow localization during tensile loading proceeds in such a manner that the temporal stages of deformation are distributed spatially along the length of the specimen.

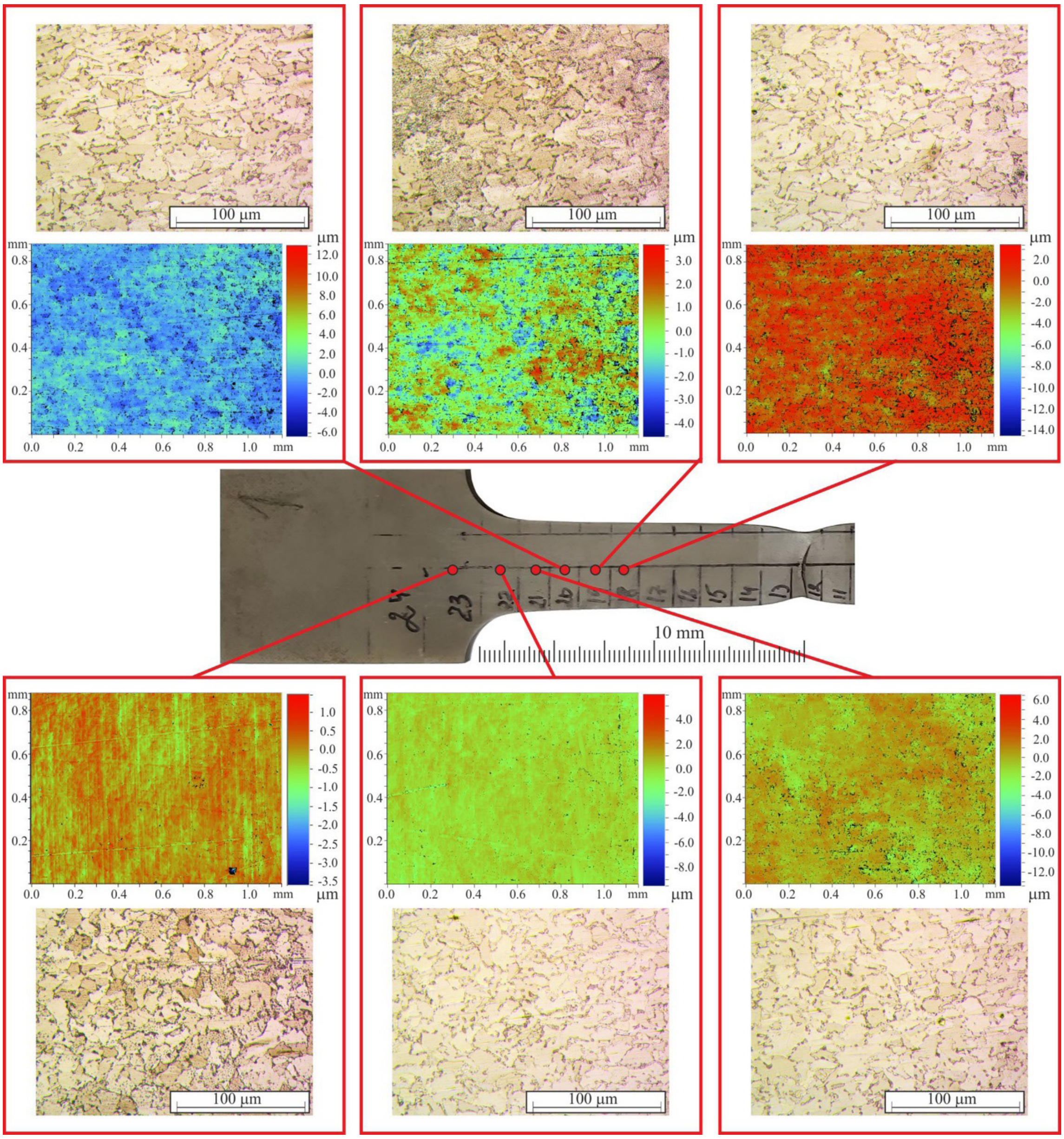

Fig. 10. Microstructure and topographic image of the specimen surface after uniaxial tension at points 18–23

This principle enabled the assignment of each specific equivalent strain value to a corresponding fixed location along the specimen.

Surface roughness measurements were performed before and after tensile testing, both along the entire gauge length and on the grip heads of the specimen, which remained undeformed during loading.

The plastic strain magnitude (curve 3 in Fig. 12) corresponds to changes in the surface relief height, with the maximum values observed within the plastic strain localization zone. The roughness parameters ***Ra*** and ***Rq*** (curves 1 and 2 in Fig. 12) reach their maxima at the specimen center and within the region of localized plastic deformation, while decreasing toward the undeformed sections located on the grip heads. A sharp drop in roughness parameters is observed within the transition zone outside the specimen gauge length. Within the undeformed areas, the roughness values correspond to their initial states.

This evolution of roughness parameters is driven by changes in surface topography associated with the emergence of defects at the specimen surface, the formation of a cellular substructure, as well as grain rotation and fragmentation — features that are characteristic of deformation localization at the mesoscale. Based on the data obtained for specimen 2, it can be inferred that the plastic strain localization zones originate near measurement areas 6 and 7.

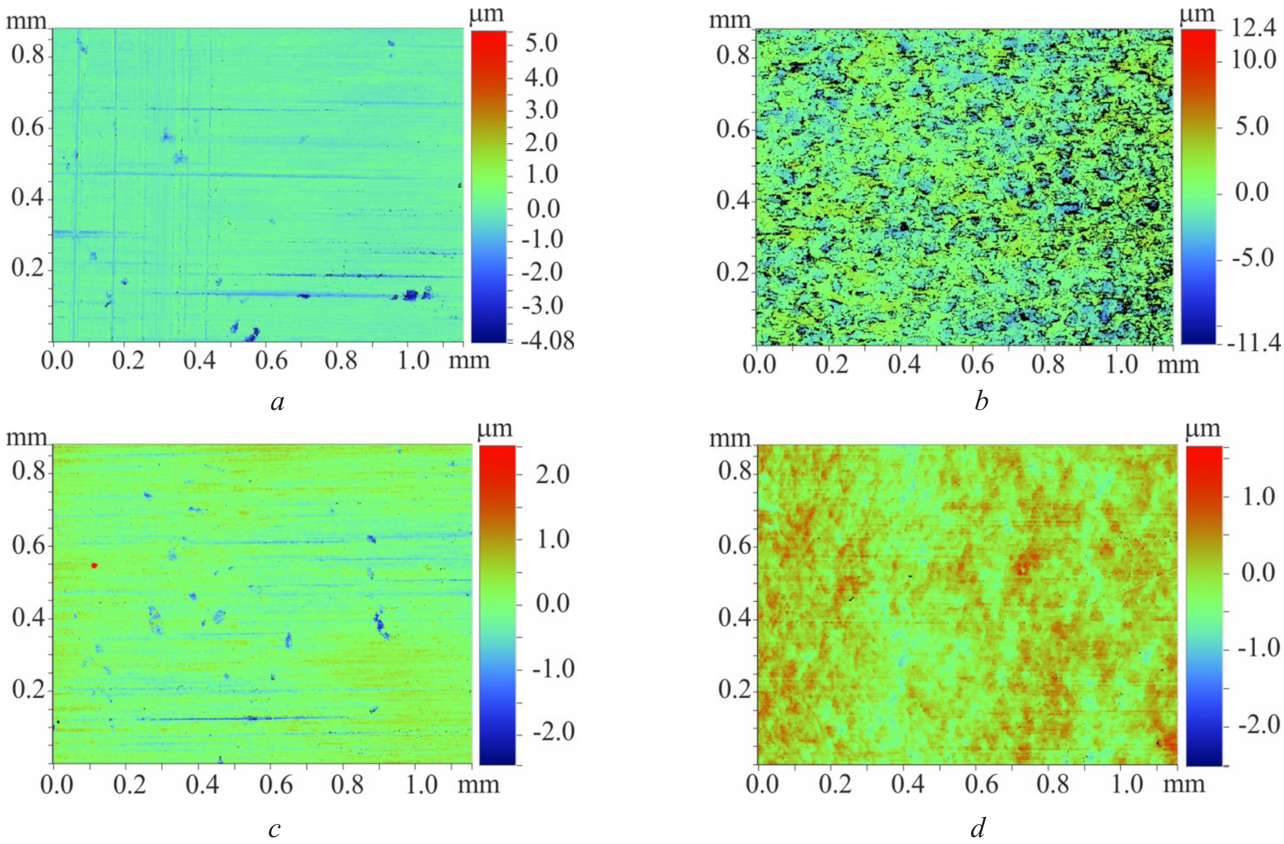

Fig. 11. Topographic images of the surface of specimen 2 before (*a*, *c*) and after (*b*, *d*) uniaxial tension in the center (*a*, *b*) and on the heads, outside the gripping zone (*c*, *d*)

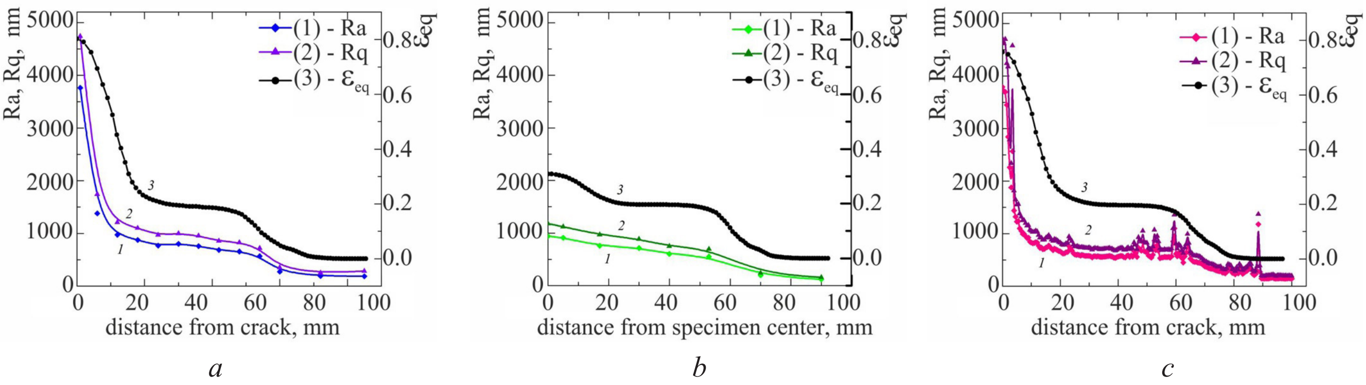

Fig. 12. Distribution of roughness parameters ***Ra*** and ***Rq*** and equivalent strain ε_{eq} along the specimen axis: from the fracture site (*a* – specimen 1, *c* – specimen 3) and from the specimen center (*b* – specimen 2) to the undeformed zone at the specimen heads

For the roughness profiles shown in Figs. 12,*a* and 12,*b*, measurements were performed along the axis with a 5 mm step, whereas for curve 3 (Fig. 12,*c*), the step was reduced to 0.25 mm. This finer resolution enabled the registration of not only roughness variations but also the relief waves induced by Lüders–Chernov bands. To provide clearer visualization, continuous topography mapping of the central surface band of specimen 3 with a width of 0.88 mm was carried out at a distance of 40–60 mm from the crack, as presented in Fig. 13,*a*. In this region, relief macrowaves oriented at an angle of approximately 45° to the specimen axis are clearly observed. Fig. 13 illustrates the general view of specimen 3 after deformation, where macro-shear bands are clearly visible to the unaided eye.

Roughness measurements enable the evaluation of both the strain degree and the deformation stage, allowing the yield plateau, uniform deformation stage, localized deformation stage, and softening stage to be clearly distinguished (Fig. 14).

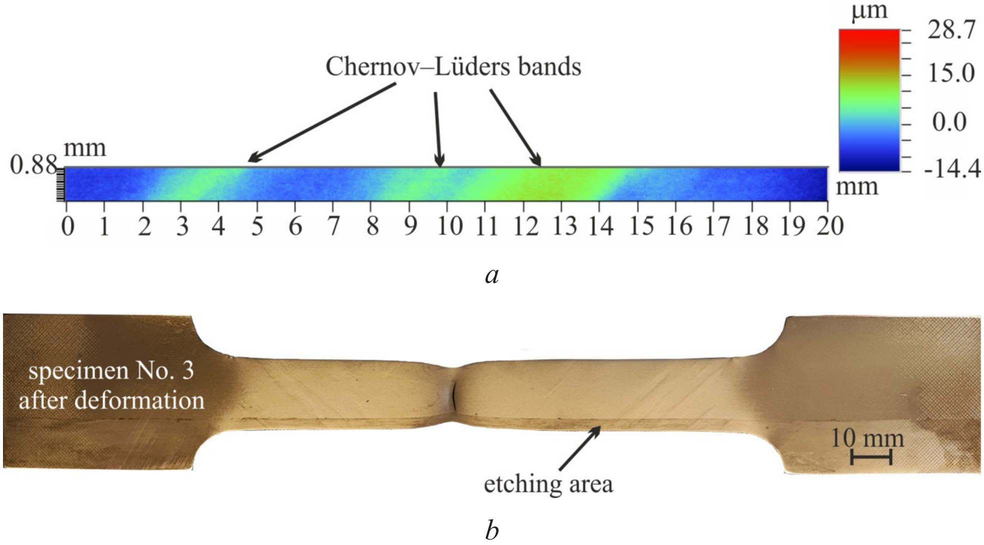

Fig. 13. Topographic image of the specimen surface (*a*) and general view (*b*) of specimen 3

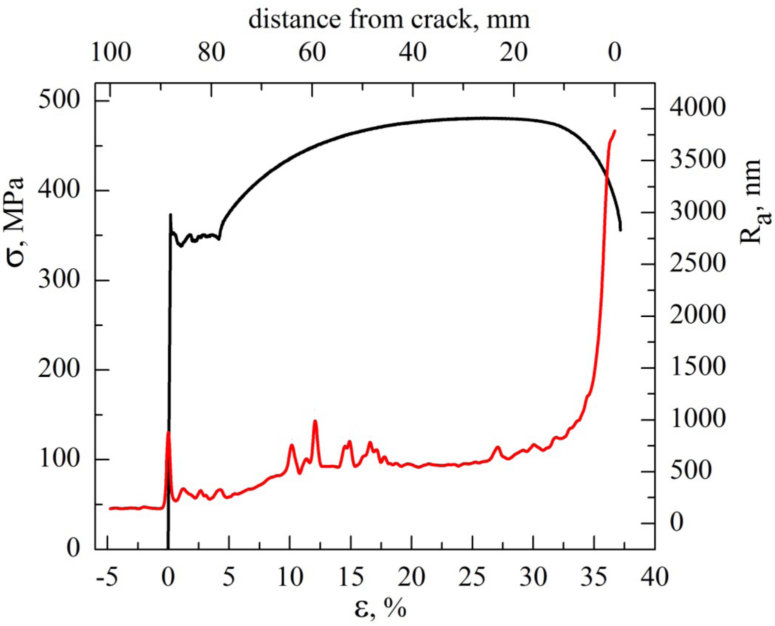

Fig. 14. Correlation between the stress–strain state and the ***Ra*** parameter for specimen 3

The implemented methodological approach consists of measuring surface roughness parameters and micromechanical characteristics continuously along the tensile axis of a specimen stretched until failure-ranging from the main crack (the zone of maximum post-critical deformation in the neck) to the undeformed section of the grip head. Using mathematical modeling based on the tensile curve, a continuous distribution function of the true strain along the specimen axis was reconstructed. Unlike numerous studies in which roughness parameters are measured discretely at fixed deformation increments, the approach utilized in this work enabled tracing the kinetics of deformation relief evolution across the entire loading diagram up to failure.

A study of the mechanical characteristics via instrumented microindentation was conducted on individual sections of the specimen after uniaxial tension. Fig. 15 illustrates the spatial dependencies of the *Martens* hardness, ***HM*** (*a*), indentation hardness, $\boldsymbol{H_{IT}}$ (*b*), maximum indentation depth, $\boldsymbol{h_{max}}$ (*c*), residual indentation depth, $\boldsymbol{h_p}$ (*d*), elastic work of indentation, $\boldsymbol{W_e}$ (*e*), and total mechanical work of indentation, $\boldsymbol{W_t}$ (*f*). In these plots, curve 1 represents the measured mechanical characteristic, while curve 2 shows the distribution of the strain degree.

Instrumented microindentation is a modern technique for assessing mechanical properties [37, 38]. This method enables the evaluation of mechanical characteristics in materials for which standard compression, tension, or bending tests cannot be performed [39–41].

Fig. 15 shows that as the distance from the crack increases, the maximum and residual indentation depths increase, while the *Martens* hardness ***HM*** and the indentation hardness at maximum load H_{IT} decrease. The total mechanical work of indentation (Fig. 15,*f*) corresponds to the integral under the load–displacement curve. Near the crack, the loss of ductility due to plastic deformation reduces the indentation work more significantly than the strength increase enhances it. As the distance from the crack increases, the indentation work grows. Conversely, the elastic indentation work decreases with increasing distance from the crack. This parameter depends on the hardness-to-elastic modulus ratio; a higher ratio implies that more work is expended on elastic deformation, thereby releasing more elastic energy during unloading. The sharp increase in both H_{IT} and ***HM***, along with the decreased indentation depth, is driven by the rising defect density and the development of the deformation structure. As seen in Fig. 16, the contact elastic modulus depends weakly on the distance along the specimen axis, which is consistent with the fact that the elastic modulus of a metal is a structure-insensitive property.

However, the first minimum on the curve approaching the crack may be attributed to material discontinuities, namely the presence of micropores and microcracks near the macrodefect, which are clearly visible in Figs. 7,*a* and 7,*b*. The subsequent fluctuations observed in the contact elastic modulus result from the superposition of several physical factors. First, they are sensitive to the local stress gradient and the formation of deformation textures. Second, the local rearrangement of substructures leads to both the redistribution of internal stresses and the cooperative reorientation (rotations) of structural elements. This process induces anisotropy, thereby either maximizing or minimizing the ***E**** value. Moreover, the extrema (minima) on the curve cannot be maintained solely by lattice rotation. The second minimum of the contact

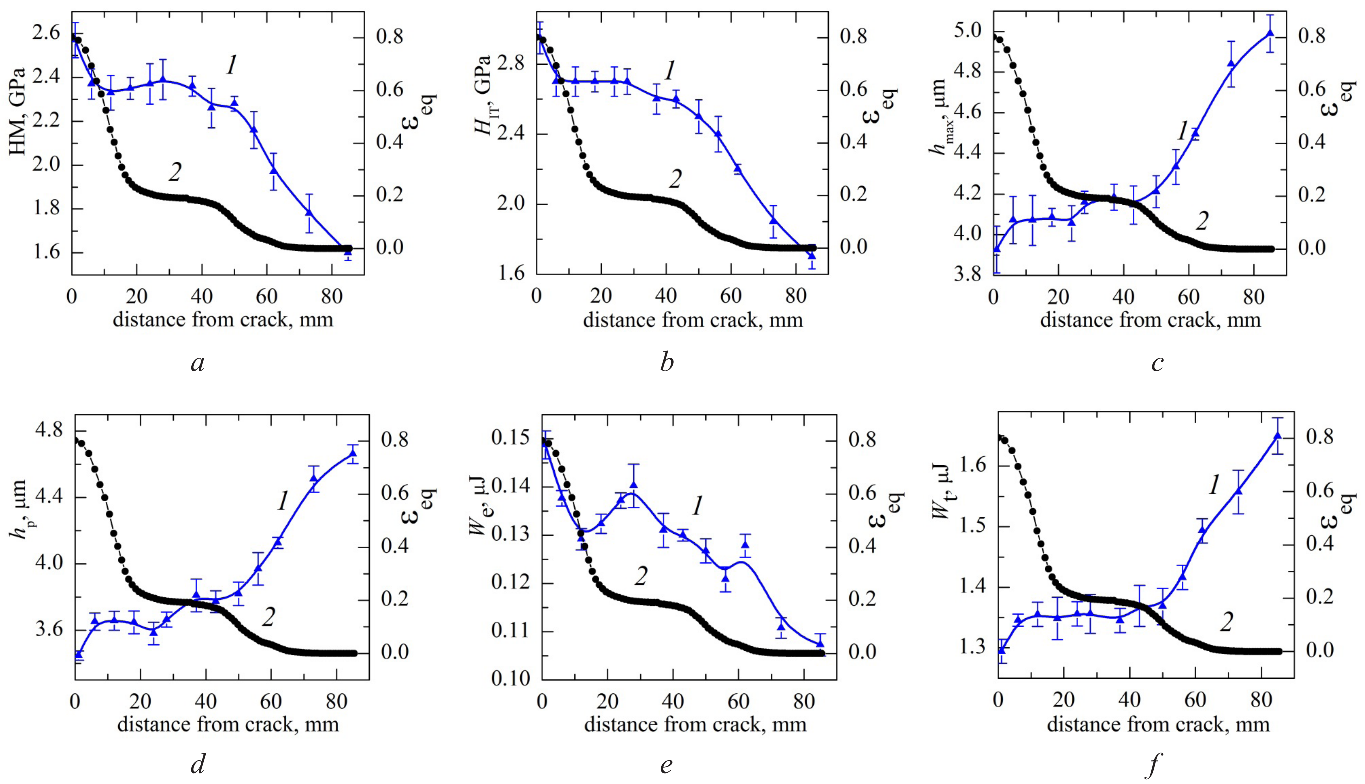

Fig. 15. Effect of distance from the fracture site on: *Martens* hardness ***HM*** (*a*), indentation hardness at maximum load H_{IT} (*b*), maximum indentation depth h_{max} (*c*), residual indentation depth h_p (*d*), elastic indentation work W_e (*e*), and total indentation work W_t (*f*)

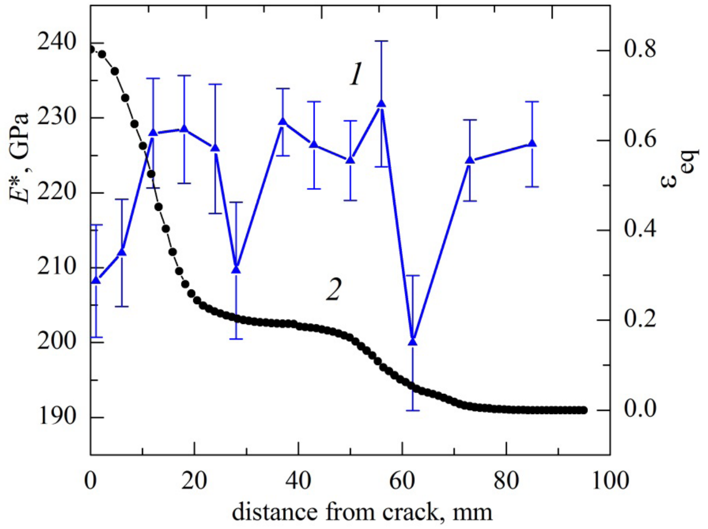

Fig. 16. Effect of distance from the fracture site on the indentation modulus ***E****

elastic modulus curve corresponds to the location where the applied stress reaches the ultimate tensile strength, marking the onset of localized plastic deformation. The appearance of a minimum at a distance greater than 60 mm is likely due to a dislocation substructure distinct from the surrounding volume. Up to this extremum, an ordered cellular substructure is observed, since at distances greater than 70 mm, the material structure remains virtually unaffected by deformation. Within the localized zone itself, the density of randomly distributed crystal lattice imperfections increases sharply, creating so-called dislocation chaos. The obtained results are in good agreement with the classification presented in [4].

The increase in the density of randomly distributed dislocations is confirmed by the *EBSD* analysis results. Since the material did not undergo actual recrystallization during testing, these maps were utilized to quantify the fractions of undeformed grains, deformed grains, and subgrains. On these maps, blue corresponds to undeformed grains, red to deformed grains, and yellow to subgrains.

The fractions of recrystallized grains, deformed grains, and subgrains were plotted as functions of the strain degree (Fig. 19,*a*) and the distance from the crack (Fig. 19,*b*).

At a distance of approximately 60 mm from the crack, a sharp increase in the subgrain fraction is observed, which correlates well with the data shown in Fig. 18. Closer to the crack, at a distance of 30 mm, deformed grains predominate, indicating a transition in the dislocation substructure from cellular to fragmented (Fig. 17). Both the *EBSD* maps and the microindentation results, which revealed changes in the substructure type, proved highly informative for identifying individual deformation stages. Together, these complementary findings enable an accurate assessment of the material's deformation history.

Conclusion

In this study, a comprehensive structural and micromechanical investigation was performed on *0.09C-2Mn-Si* structural steel specimens subjected to uniaxial tension. The experimental approach integrated instrumented indentation, surface profilometry, optical microscopy, and scanning electron microscopy.

Optical profilometry revealed a clear correlation between surface roughness parameters and the degree of strain, with the evolution of surface relief reflecting distinct zones of localized plastic deformation at the mesoscale. Roughness measurements were shown to enable assessment of both the strain magnitude and the corresponding deformation stage, allowing clear differentiation of the yield plateau, uniform elongation, localized deformation, and softening stages.

Optical metallography revealed progressive elongation of ferrite grains with increasing strain; however, qualitative microstructural changes – such as the formation of elongated, fragmented grains and the crushing of pearlite colonies – could only be detected within the localized deformation zone. In contrast, *EBSD* analysis proved effective in characterizing the substructural evolution of the deformed metal.

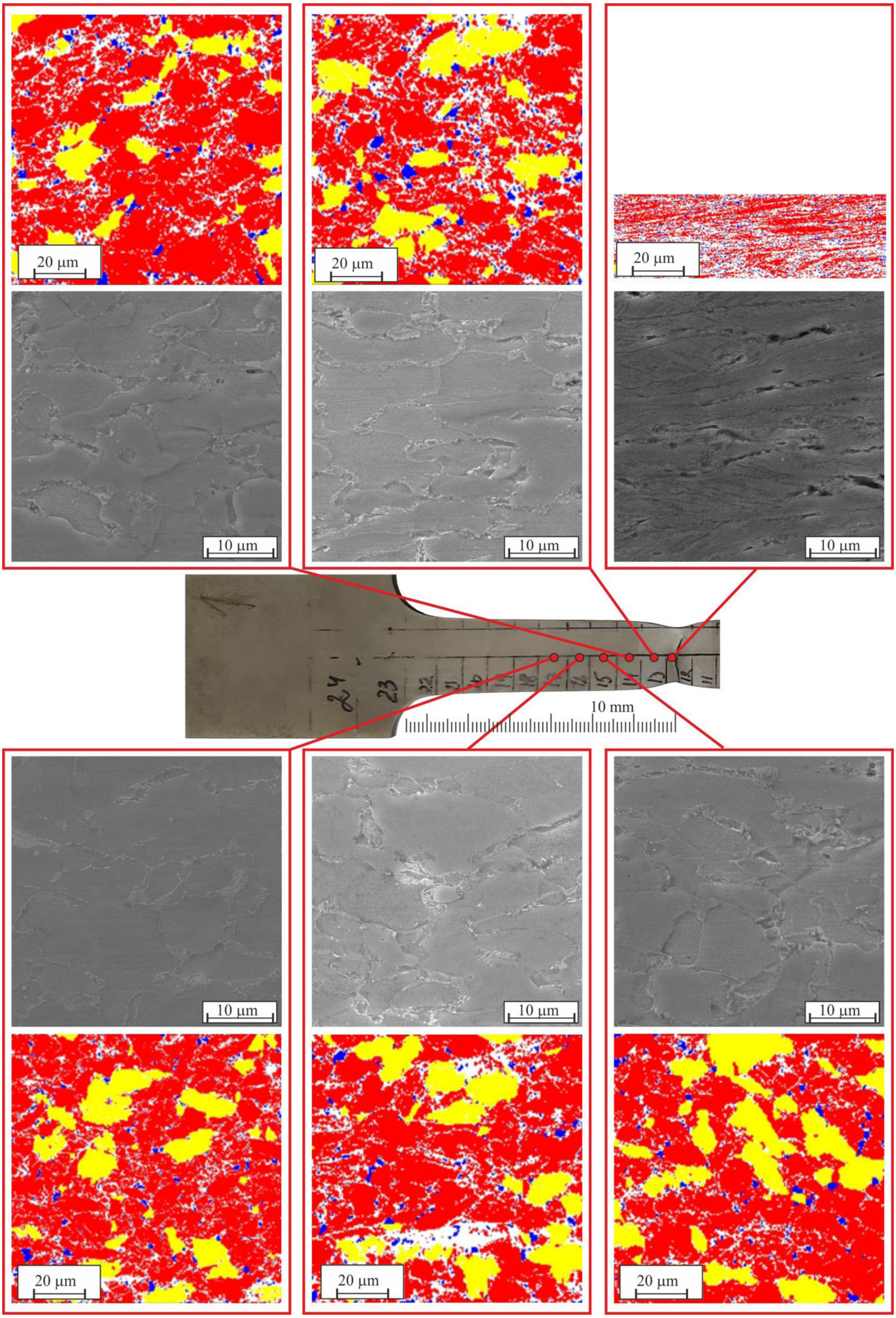

Fig. 17. Microstructure and *EBSD* orientation maps of specimen 1 after uniaxial tension at points 12–17

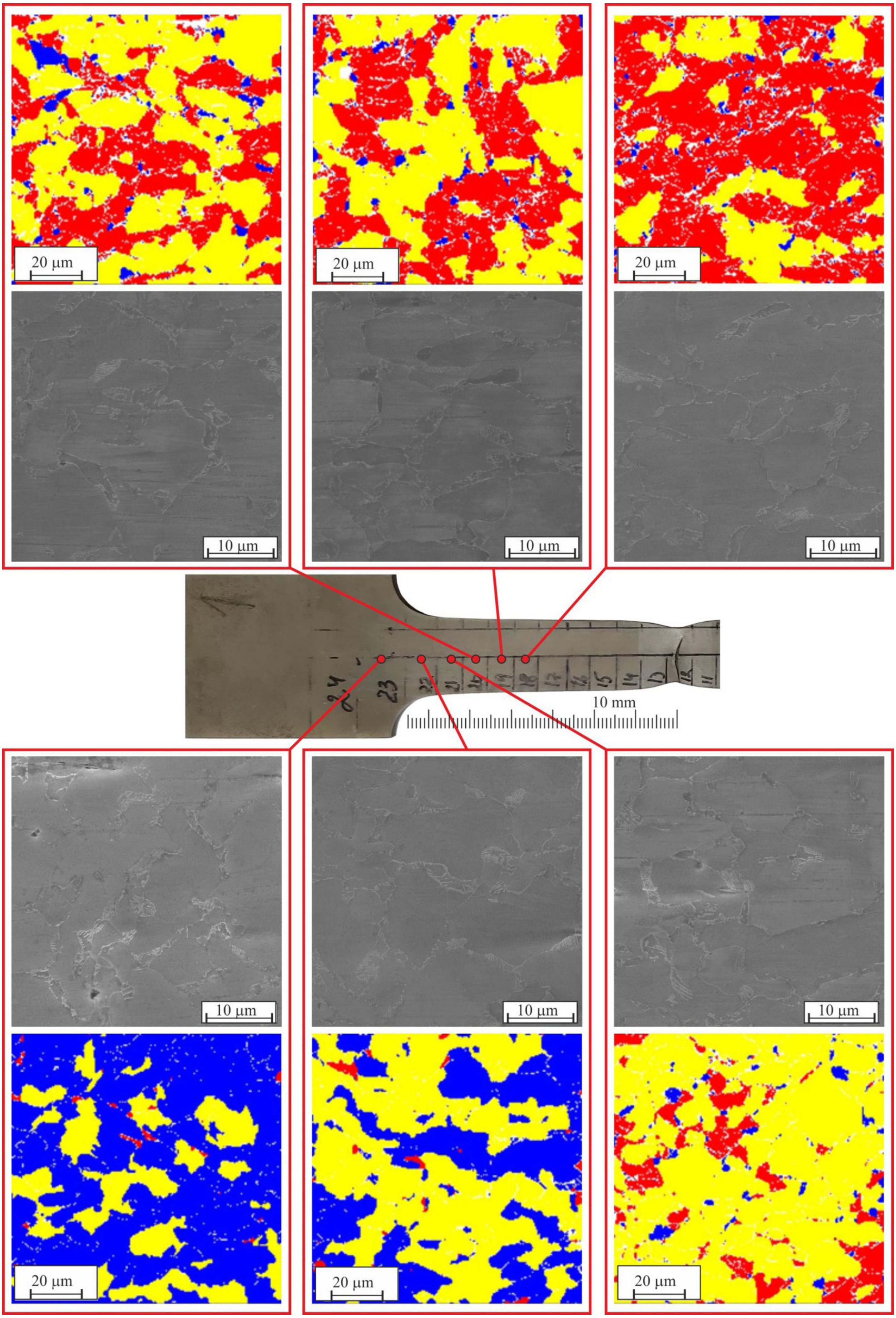

Fig. 18. Microstructure and *EBSD* orientation maps of specimen 1 after uniaxial tension at points 18–23

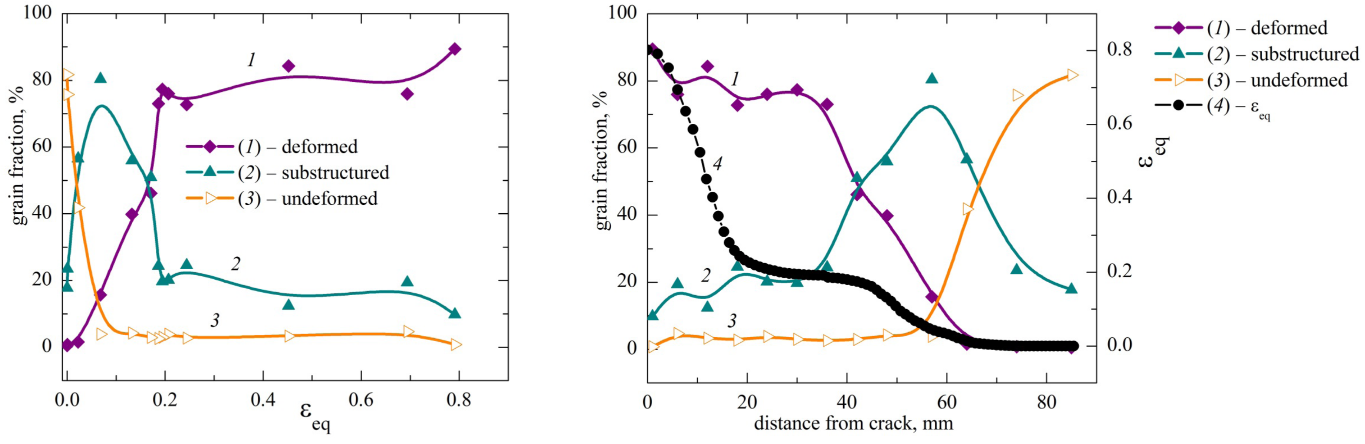

a *b*

Fig. 19. Grain fraction as a function of equivalent strain (*a*) and of distance from the crack (*b*) for the specimen after uniaxial tension

The results demonstrate the fundamental feasibility of assessing the strain degree in *0.09C-2Mn-Si* steel through analysis of its microstructural parameters, micromechanical properties, and mesorelief. Quantitative correlations governing the variations in microstructure, mechanical properties, and surface roughness as functions of strain were established. The obtained empirical relationships provide a foundation for the development of non-destructive testing methods. Nevertheless, the authors emphasize that the application of these findings to real-world engineering components will require accounting for the structural and chemical heterogeneity inherent to industrial rolled products, as well as the collection of a sufficiently extensive statistical dataset.

For the *0.09C-2Mn-Si* low-alloy steel under investigation, a continuous evolution of surface topography was established across the entire stress–strain diagram. A non-monotonic dependence of surface roughness on the strain degree was revealed, attributed to a reversal in the roughness increment during the transition from uniform plastic flow to macrolocalized deformation within the neck and at the immediate pre-fracture stages.

It was established that near the crack, where the highest strain levels are concentrated, the microstructure is devoid of distinct pearlite colonies. Instead, it is characterized by elongated ferrite grains, the boundaries of which are occasionally decorated by fragmented cementite platelets. Discontinuities and elongated deformation-induced pores are clearly visible, while the surface relief is governed by slip along meso- and macro-shear bands.

References

1. Koneva N.A. Priroda stadii plasticheskoi deformatsii [The nature of plastic deformation stages]. *Sorosovskii obrazovatel'nyi zhurnal = Soros Education Journal*, 1998, vol. 4, no. 10, pp. 99–105. (In Russian).

2. Panin V.E., Grinyaev Yu.V., Elsukova T.F., Ivanchin A.G. Structural levels of deformation in solids. *Soviet Physics Journal*, 1983, vol. 25 (6), pp. 479–497. DOI: 10.1007/BF00898745.

3. Panin V.E., Panin A.V. Fundamental role of nanoscale structural level of plastic strain in solids. *Metal Science and Heat Treatment*, 2006, vol. 48 (11–12), pp. 533–538. DOI: 10.1007/s11041-006-0131-x.

4. Koneva N.A. Klassifikatsiya, evolyutsiya i samoorganizatsiya dislokatsionnykh struktur v metallakh i splavakh [Classification, evolution and self-organization of dislocation structures in metals and alloys]. *Sorosovskii obrazovatel'nyi zhurnal = Soros Education Journal*, 1996, vol. 2, no. 6, pp. 99–107. (In Russian).

5. Panin V.E., Panin A.V. Masshtabnye urovni plasticheskoi deformatsii razrusheniya nanostrukturirovannykh materialov [Scale levels of plastic deformation and fracture of nanostructured materials]. *Nanotekhnika*, 2005, no. 3, pp. 28–42. (In Russian).

6. Rybin V.V. *Bol'shie plasticheskie deformatsii i razrushenie metallov* [Large plastic deformations and fracture of metals]. Moscow, Metallurgiya Publ., 1986. 224 p.

7. Panin V.E., Grinyaev Yu.V., Danilov V.I. *Strukturnye urovni plasticheskoi deformatsii i razrusheniya* [Structural levels of plastic deformation and fracture]. Novosibirsk, Nauka Publ., 1990. 255 p. ISBN 5-02-029308-3.

8. Koneva N.A., Kozlov E.V., Trishkina L.I., Pekarskaya E.E. Thermodynamics of substructure transformations under plastic deformation of metals and alloys. *Materials Science and Engineering: A*, 1997, vol. 234–236, pp. 614–616. DOI: 10.1016/S0921-5093(97)00271-2.

9. Koneva N.A., Kozlov E.V., Trishkina L.I., Zhdanov A.N. Mekhanizmy uprochneniya i osobennosti stadiinosti deformatsii polikristallov s nanozernom [Mechanism of strength and features stageness deformations of polycrystalline materials with ultrafine grain]. *Deformatsiya i razrushenie materialov*, 2009, no. 1, pp. 12–15. (In Russian).

10. Panin V.E., Egorushkin V.E., Panin A.V. Fizicheskaya mezomekhanika deformiruemogo tverdogo tela kak mnogourovnevoi sistemy. 1. Fizicheskie osnovy mnogourovnevogo podkhoda [Physical mesomechanics of a deformed solid as a multilevel system. I. Physical fundamentals of the multilevel approach]. *Fizicheskaya mezomekhanika = Physical Mesomechanics*, 2006, vol. 9, no. 3, pp. 9–22. (In Russian).

11. Adamov A.A., Keller I.E., Petukhov D.S. Eksperimental'naya identifikatsiya zakonov plastichnosti i razrusheniya anizotropnoi malouglerodistoi listovoi stali dlya modelirovaniya kholodnoi shtampovki [Experimental identification of plasticity and fracture laws for anisotropic low-carbon sheet steel for cold stamping simulation]. *Problemy prochnosti i plastichnosti = Problems of Strength and Plasticity*, 2019, vol. 81, no. 2, pp. 202–211. DOI: 10.32326/1814-9146-2019-81-2-202-211. (In Russian).

12. Tabatchikova T.I., Tereshchenko N.A., Yakovleva I.L., Gudnev N.Z. Structure of near-surface layer of high-strength steel subjected to abrasive waterjet cutting. *Physics of Metals and Metallography*, 2018, vol. 119 (9), pp. 871–879. DOI: 10.1134/S0031918X18090107.

13. Bataev I.A., Bataev A.A., Balagansky I.A., Burov V.G., Prikhodko E.A., Moreva N.A., Ruktuev A.A. Localization of plastic flow in low-carbon steel deformed by explosion. *Physical Mesomechanics*, 2011, vol. 14, no. 1, pp. 93–99. DOI: 10.1134/S102995991101011X. Translated from *Fizicheskaya mezomekhanika*, 2011, vol. 14, no. 1, pp. 93–99.

14. Kopanitsa D.G., Ustinov A.M., Potekaev A.I., Klopotov A.A. Evolyutsiya strukturnykh elementov deformatsii v pripoverkhnostnykh sloyakh obraztsov iz nizkolegirovannoi stali [Evolution of structural elements of deformation in near-surface layers of low-alloy steel specimens]. *Sovremennye problemy teorii mashin = Modern problems of the theory of machines*, 2015, no. 3, pp. 218–223.

15. Bowden H.G., Kelly P.M. Deformation twinning in shock-loaded pearlite. *Acta Metallurgica*, 1967, vol. 15 (1), pp. 105–111. DOI: 10.1016/0001-6160(67)90158-7.

16. Pröger M. *Die Deformations und Bruchmechanismen des lamellaren Perlits*. Dissertation. Stuttgart, 1964. 101 p.

17. Tushinsky L.I., Bataev A.A., Tikhomirova L.B. *Struktura perlita i konstruktivnaya prochnost' stali* [Pearlite structure and constructive strength of steel]. Novosibirsk, Nauka Publ., 1993. 280 p. ISBN 5-02-030323-2.

18. Bataev A.A., Tushinskii L.I., Bataev V.A., Zuev L.B. Features of the plastic deformation of steels with a lamellar pearlite structure. *Russian Physics Journal*, 1996, vol. 39 (7), pp. 603–608. DOI: 10.1007/BF02439086.

19. Bataev V.A., Bataev A.A., Kotorov S.A., Tushinskii L.I. Special features of the fracture of ordered segregated excess cementite in eutectoid steels. *Metal Science and Heat Treatment*, 1999, vol. 41 (3–4), pp. 101–104. DOI: 10.1007/BF02467693.

20. Bataev I.A., Bataev A.A., Esikov M.A., Dostovalov R.A., Belousova N.S. Forma mezhsloinykh granits v soedineniyakh, poluchennykh svarkoi metallicheskikh plastin The form of the interfaces obtained by explosive welding of thin-plate metalic materials]. *Nauchnyi vestnik Novosibirskogo gosudarstvennogo tekhnicheskogo universiteta = Science Bulletin of the Novosibirsk State Technical University*, 2012, no. 4 (49), pp. 107–112.

21. Panin V.E. Overview on mesomechanics of plastic deformation and fracture of solids. *Theoretical and Applied Fracture Mechanics*, 1998, vol. 30 (1), pp. 1–11. DOI: 10.1016/S0167-8442(98)00038-X.

22. Panin V.E. Synergistic principles of physical mesomechanics. *Theoretical and Applied Fracture Mechanics*, 2001, vol. 37 (1), pp. 261–298. DOI: 10.1016/S0167-8442(01)00085-4.

23. Panin V.E., Derevyagina L.S., Deryugin E.E., Panin A.V., Panin S.V., Antipina N.A. Zakonomernosti stadii predrazrusheniya v fizicheskoi mezomekhanike [Regularities of the fracture nucleation stage in physical mesomechanics]. *Fizicheskaya mezomekhanika = Physical Mesomechanics*, 2003, vol. 6, no. 6, pp. 97–106. (In Russian).

24. Likhachev V.A., Panin V.E., Zasimchuk E.E. *Kooperativnye deformatsionnye protsessy i lokalizatsiya deformatsii* [Cooperative deformation processes and deformation localization]. Kiev, Naukova Dumka Publ., 1989. 320 p. ISBN 5-12-001121-7.

25. Panin V.E., ed. *Fizicheskaya mezomekhanika i komp'yuternoe konstruirovanie materialov*. V 2 t. T. 2 [Physical mesomechanics and computer-aided design of materials. In 2 vol. Vol. 2]. Novosibirsk, Nauka Publ., 1995. 320 p. ISBN: 5-02-030841-2.

26. Hatherley M., Malin A.S. Shear bands in deformed metals. *Scripta Metallurgica*, 1984, vol. 18 (5), pp. 449–454. DOI: 10.1016/0036-9748(84)90419-8.

27. Harren S.V., Dève H.E., Asaro R.J. Shear band formation in plane strain compression. *Acta Metallurgica*, 1988, vol. 36 (9), pp. 2435–2480. DOI: 10.1016/0001-6160(88)90193-9.

28. Panin V.E., Egorushkin V.E., Panin A.V., Moiseenko D.D. On the nature of plastic strain localization in solids. *Technical Physics*, 2007, vol. 52 (8), pp. 1024–1030. DOI: 10.1134/S1063784207080105.

29. Zuev L.B., Khon Yu.A. Plastic flow as spatiotemporal structure formation. Part I. Qualitative and quantitative patterns. *Physical Mesomechanics*, 2022, vol. 25 (2), pp. 103–110. DOI: 10.1134/S1029959922020011.

30. McDowell D.L. Multiscale modeling of interfaces, dislocations, and dislocation field plasticity. Mesarovic S., Forest S., Zbib H. (eds.). *Mesoscale Models. CISM International Centre for Mechanical Sciences*. Cham, Springer International Publishing, 2019, vol. 587, pp. 195–297. DOI: 10.1007/978-3-319-94186-8_5.

31. Trusov P.V., Shveykin A.I. *Mnogourovnevye modeli mono- i polikristallicheskikh materialov: teoriya, algoritmy, primery primeneniya* [Multilevel models of mono- and polycrystalline materials: theory, algorithms, application examples]. Novosibirsk, SB RAS Publ., 2019. 605 p. ISBN 978-5-7692-1661-9. DOI: 10.15372/MULTILEVEL2019TPV.

32. Panin V.E. Osnovy fizicheskoi mezomekhaniki [Foundations of physical mesomechanics]. *Fizicheskaya mezomekhanika = Physical Mesomechanics*, 1998, vol. 1, no. 1, pp. 5–22. (In Russian).

33. Panin V.E., Grinyaev Yu.V. Fizicheskaya mezomekhanika – novaya paradigma na styke fiziki i mekhaniki deformiruemogo tverdogo tela [Physical mesomechanics: a new paradigm at the interface of solid state physics and solid mechanics]. *Fizicheskaya mezomekhanika = Physical Mesomechanics*, 2003, vol. 6, no. 4, pp. 9–36. (In Russian).

34. Trusov P.V., Shveykin A.I., Kondratyev N.S., Yants A.Yu. Multilevel models in physical mesomechanics of metals and alloys: results and prospects. *Physical Mesomechanics*, 2021, vol. 24 (4), pp. 391–417. DOI: 10.1134/S1029959921040056.

35. Khudorozhkova Yu.V., Povolotskaya A.M., Burov S.V., Vichuzhanin D.I. Applicability of magnetic measurements to the detection of fracture nucleation in 09G2S steel. *Russian Journal of Nondestructive Testing*, 2025, vol. 61 (12), pp. 1477–1487. DOI: 10.1134/S1061830925700457.

36. Smirnov S.V., Smirnov V.K., Soloshenko A.N., Shveikin V.P. Determining the coefficients in the functional dependence of the strain resistance on the basis of conical-indentor data. *Russian Metallurgy (Metally)*, 1998, no. 6, pp. 109–113.

37. Makarov A.V., Savrai R.A., Gorkunov E.S., Yurovskikh A.S., Malygina I.Yu., Davydova N.A. Structure, mechanical characteristics, and deformation and fracture features of quenched structural steel under static and cyclic loading after combined strain-heat nanostructuring treatment. *Physical Mesomechanics*, 2015, vol. 18 (1), pp. 43–57. DOI: 10.1134/S1029959915010063.

38. Soboleva N.N., Makarov A.V., Stepchenkov A.K., Malygina I.Yu., Korobov Yu.S. Vliyanie termicheskogo vozdeistviya na mikromekhanicheskie svoistva khromonikelevogo pokrytiya, poluchennogo gazoporoshkovoi lazernoi naplavkoi [Influence of thermal effects on the micromechanical properties of the nickel-chromium coating obtained by gas powder laser cladding]. *Obrabotka metallov (tekhnologiya, oborudovanie, instrumenty)= Metal Working and Material Science*, 2020, vol. 22, no. 2, pp. 104–117. DOI: 10.17212/1994-6309-2020-22.2-104-117.

39. Oreshko E.I., Erasov V.S., Yakovlev N.O., Utkin D.A. Metody opredeleniya mekhanicheskikh kharakteristik materialov s pomoshch'yu indentirovaniya (obzor) [Methods for determining the mechanical characteristics of materials using indentation (review)]. *Aviatsionnye materialy i tekhnologii = Aviation Materials and Technologies*, 2021, no. 1 (62), pp. 104–118. DOI: 10.18577/2713-0193-2021-0-1-104-118. (In Russian).

40. Soboleva N.N., Davydova N.A., Makarov A.V. Vliyanie kratnosti friktsionnogo vozdeistviya na mikromekhanicheskie svoistva NiCrBSi-pokrytii [The effect of the multiplicity of frictional action on the micromechanical properties of NiCrBSi-coatings]. *Diagnostics, Resource and Mechanics of Materials and Structures*, 2022, iss. 5, pp. 50–59. DOI: 10.17804/2410-9908.2022.5.050-059. (In Russian).

41. Pugacheva N.B., Bykova T.M., Senaeva E.I. Struktura i mikromekhanicheskie svoistva SVS-kompozitov s mednoi matritsei: osobennosti formirovaniya [Structure and micromechanical properties of SHS composites with a copper matrix: peculiarities of formation]. *Frontier Materials & Technologies*, 2023, no. 4, pp. 99–108. DOI: 10.18323/2782-4039-2023-4-66-9. (In Russian).

Conflicts of Interest

The authors declare no conflict of interest.